J Mater Sci (2016) 51:603–614
DOI 10.1007/s10853-015-9315-3

50TH ANNIVERSARY

Pd-based nanoflowers catalysts: controlling size, composition, and structures for the 4-nitrophenol reduction and BTX oxidation reactions

Anderson G. M. da Silva[1] · Thenner S. Rodrigues[1] · Laís S. K. Taguchi[1] · Humberto V. Fajardo[2] · Rosana Balzer[3] · Luiz F. D. Probst[3] · Pedro H. C. Camargo[1]

Received: 14 May 2015 / Accepted: 30 July 2015 / Published online: 7 August 2015

Abstract We describe herein the synthesis of solid Au@Pd and hollow AgPd nanoflowers displaying controlled sizes and compositions in order to investigate how their size, composition, and the presence of Au in the core of the nanoparticles influence their catalytic performance toward both liquid and gas-phase transformations. While the size and composition of Au@Pd and AgPd the nanoflowers could be controlled as function of growth time, their structure (solid or hollow) was dependent on the nature of the seeds employed for the synthesis, i.e., Au or Ag nanoparticles. Moreover, Au@Pd and AgPd nanoflowers were successfully supported onto commercial silica displaying truly uniform dispersion. The catalytic activities of Au@Pd and AgPd nanoflowers were investigated toward the 4-nitrophenol reduction and the benzene, toluene, and *o*-xylene (BTX) oxidation. The catalytic activities for the reduction of 4-nitrophenol decreased as follows: $Au_{58}@Pd_{42} > Au_{27}@Pd_{73} > Ag_{20}Pd_{80}$ and $Ag_8Pd_{92} > Au_{12}@Pd_{88} > Ag_{38}Pd_{62}$, suggesting that the Au core enhanced the catalytic activity relative to the hollow material when for Pd at.% was up to 80. Regarding the BTX oxidation, supported Au@Pd displayed higher catalytic activities than AgPd nanoflowers, also illustrating the role of the Au cores in the nanoflowers for improving catalytic performance. We believe these results may serve as a platform for the synthesis of Pd-based bimetallic nanomaterials that enable the correlation between these physical/chemical parameters and properties and thus optimized catalytic activities.

Introduction

Palladium (Pd) nanostructures have been employed as catalysts for a variety of transformations that include oxidation, hydrogenation, reduction, carbon–carbon coupling (Suzuki, Heck, and Stille) reactions, among others [1–6]. In catalytic applications, strategies that enable one to improve/maximize performance are of vital importance due to high costs and rare reserves of noble metals such as Pd. For instance, catalytic properties can be optimized by maneuvering size, shape (control over exposed surface facets), composition, and structure (solid vs. hollow interiors) in metal nanocrystals [7–13]. Hollow interiors, for example, may enable higher surface areas relative to their solid analogs [14]. Also, it has been demonstrated that bimetallic compositions containing Pd (including Pd–Au and Pd–Ag combinations) have led to improved in catalytic activities toward oxidation and reduction reactions as compared to monometallic nanoparticles due to the synergism/combination of properties between the metal components [12, 15–20].

Nevertheless, a precise correlation between performance and many of the physical and chemical parameters that define the catalyst (size, shape, composition and structure) is crucial to design nanostructures with desired properties and optimized performances. This remains challenging, as it requires

Electronic supplementary material The online version of this article (doi:10.1007/s10853-015-9315-3) contains supplementary material, which is available to authorized users.

✉ Pedro H. C. Camargo
camargo@iq.usp.br

[1] Departamento de Química Fundamental, Instituto de Química, Universidade de São Paulo, Av. Prof. Lineu Prestes, 748, São Paulo, SP 05508-000, Brazil

[2] Departamento de Química, Universidade Federal de Ouro Preto, Ouro Preto, MG 35400-000, Brazil

[3] Departamento de Química, Universidade Federal de Santa Catarina, Florianópolis, SC 88040-900, Brazil

uniform nanomaterials in which several of these parameters must be controlled [21]. Moreover, practical applications in heterogeneous catalysis require active species to be deposited onto a solid support, as agglomeration may take place during the utilization of the unsupported nanoparticles [22, 23]. This demands the synthesis of controlled nanostructures in relatively large amounts. Still, several protocols for the controlled synthesis of nanomaterials are limited regarding their large-scale applicability [24, 25].

In this paper, we describe a facile strategy for synthesis of bimetallic nanomaterials containing Pd. More specifically, we focused on the synthesis of solid Au@Pd (core@shell) and hollow AgPd nanoflowers displaying controlled sizes and compositions followed by the investigation of their catalytic performances as a function of these parameters toward the 4-nitrophenol reduction and the benzene, toluene, and *o*-xylene (BTX) oxidation. We were interested in studying how the presence of Au in the core of the nanoparticles influences their catalytic performance toward both liquid and gas-phase transformations. In this context, the use of Ag and Au as templates represents an intuitive strategy as Ag leads to hollow interiors, while Au lead, to solid, core–shell systems. We focused on Pd-based nanoflowers as their surface is comprised of small Pd branches/petals, making them attractive for catalytic applications as they enable one, at least in principle, to achieve higher surface areas relative to their rounded counterparts [19, 26–29]. While their size could be controlled as a function of the Pd growth time, their structure was dependent on the nature of the seeds employed for the synthesis, i.e., Au or Ag nanoparticles. Our protocol could be scaled-up by 100-folds and the resulting nanoflowers supported onto commercial silica with highly uniform dispersion. This enabled us to investigate the catalytic performance of both unsupported and supported nanoflowers (toward the 4-nitrophenol reduction and BTX oxidation, respectively). While 4-aminophenol (product from the reduction of 4-nitrophenol) represents an important intermediate in the synthesis of several analgesic and antipyretic drugs [30, 31], BTX comprise volatile organic compounds that are recognized as hazardous contaminants, and their catalytic oxidation has been acknowledged as an effective approach for their removal [32–36]. It is important to note that current challenges for the BTX oxidation include achieve substantial conversions at low temperature, avoid the formation of side products, and decrease the amount of noble metal in the catalyst.

Experimental

Materials and instrumentation

Analytical grade chemicals chloroauric acid trihydrate ($HAuCl_4{\cdot}3H_2O$, 99.9 %, Sigma-Aldrich), silver nitrate ($AgNO_3$, 99 %, Sigma-Aldrich), potassium tetrachloropalladate trihydrate ($K_2PdCl_4{\cdot}3H_2O$, 98 %, Sigma-Aldrich), polyvinylpyrrolidone (PVP, Sigma-Aldrich, M.W. 55,000 g/mol), hydroquinone ($C_6H_6O_2$, 99 %, Vetec), L-ascorbic acid ($C_6H_8O_6$, 99 %, Sigma-Aldrich), sodium borohydride ($NaBH_4$, 98 %, Sigma-Aldrich), sodium citrate dihydrate ($C_6H_5Na_3O_7{\cdot}2H_2O$, 99 %, Sigma-Aldrich), silica (pore size 22 Å, 800 m^2/g, CAS number 112926-00-8, Sigma-Aldrich), benzene (C_6H_6, >99 %, Vetec), toluene (C_7H_8, >99 %, Vetec), and *o*-xylene (C_8H_{10}, >99 %, Vetec) were used as received. The scanning electron microscopy (SEM) images were obtained using a JEOL field emission gun microscope JSM 6330F operated at 5 kV. The samples were prepared by dropcasting an aqueous suspension containing the nanostructures over a silicon wafer, followed by drying under ambient conditions. Transmission electron microscopy (TEM) images were obtained with a JEOL 1010 microscope operating at 80 kV or a JEOL JEM 2100 microscope operated at 200 kV. Samples for TEM were prepared by drop casting an aqueous suspension of the nanostructures over a carbon-coated copper grid, followed by drying under ambient conditions. UV–VIS spectra were obtained from aqueous suspensions containing the nanostructures with a Shimadzu UV-1700 or UV-3101 PC spectrophotometer. The average sizes were determined by measuring the diameter of 50 nanostructures with the quoted errors corresponding to the standard deviation of the data from the TEM images. The Au, Ag, and Pd atomic percentages were measured by flame atomic absorption spectrometry (FAAS) with a Shimadzu spectrophotometer, model AA-6300, equipped with an air-acetylene flame. Regarding the sample preparation for FAAS, a 10 mL aliquot of a suspension containing the nanoflowers was centrifuged and the supernatant was decanted. This solid, or 10 mg of the supported catalysts, were then digested with 3 mL of aqua regia, and 7 mL of water was added. This mixture was left under stirring for 1 h, and a 1 mL aliquot was employed in the analysis.

Synthesis of Au and Ag NPs seeds

Au seeds were prepared by the citrate reduction approach [37]. In a typical procedure, 30 mL of 0.25 mM $AuCl_4^-$ was added to a 100 mL round-bottom flask under magnetic stirring. This system was heated to 100 °C for 15 min, followed by the addition of 0.9 mL of 1 wt% sodium citrate dihydrate. The reaction was allowed to proceed for another 10 min, yielding a red suspension containing the Au NPs.

Ag seeds were prepared by the polyol process [38]. Briefly, 5 mg of polyvinylpyrrolidone (PVP) was dissolved in 37.5 mL of ethylene glycol. Then, $AgNO_3$ (200 mg, 1.2 mmol) was added and mixed until complete

dissolution. The resulting solution was heated to 125 °C and kept at this temperature for 2.5 h, leading to the appearance of a greenish-yellow color due to the formation of the Ag NPs. The reaction mixture was then allowed to cool to room temperature and diluted to 125 mL with water.

Synthesis of solid Au@Pd and hollow AgPd nanoflowers

Solid Au@Pd and hollow AgPd nanoflowers were synthesized by a seed-mediated growth approach. In a typical procedure, 10 or 400 μL of the as-prepared Ag or Au seeds, respectively, was added to 9.4 mL of a PVP aqueous solution (0.1 wt%). This mixture was transferred to a 25 mL round-bottom flask and stirred at 50 °C for 10 min, followed by the addition of 0.1 mL of 30 mM aqueous hydroquinone solution. After 2 min, 170 μL of a 12 mM $PdCl_4^{2-}{}_{(aq)}$ solution was added to this mixture. In order to control and monitor the growth of the produced Au@Pd and AgPd nanoflowers, the reaction was quenched at different time intervals: 15 s, 1 min, 5 min, 10 min, 30 min, and 1 h (several parallel reactions were carried out). The reactions were quenched by the addition of 0.1 mL of 0.3 M $HCl_{(aq)}$ solution to the reaction mixture and cooling to 0° C in an ice water bath. The nanostructures were isolated and washed three times with ethanol by successive rounds of centrifugation at 10000 rpm and removal of the supernatant. After washing, the nanoparticles were suspended in 10 mL of water. For the scale-up syntheses, the 25 mL round-bottom flask was replaced by a 2000-mL flask, and the volumes of all solutions were increased by a factor of 100. The formation of solid Au@Pd and hollow AgPd nanoflowers was not dependent on the presence of reducing agents, PVP, or ethylene glycol from the synthesis of Au or Ag NPs. The concentrations of the starting Ag and Au NPs suspensions were 2.16 and 0.24 mM, respectively. This corresponded to 1.2×10^{17} and 3.0×10^{15} NPs/L, respectively. The differences in the volumes of Ag and Au NPs suspensions employed during the synthesis of the nanoflowers were chosen in order to match the number of seeds/particles in each case.

Catalytic activity toward the 4-nitrophenol reduction

For the catalytic tests of the 4-nitrophenol reduction, 300 μL of a 1.4×10^{-4} M 4-nitrophenol aqueous solution, 2 mL of 4.2×10^{-2} M sodium borohydride aqueous solution, and 100 μL of the as-prepared nanoflowers were added into a quartz cuvette. Then, the change in absorbance at 400 nm was monitored by UV–Vis spectroscopy. In this case, the color of the solution gradually changed from yellow to transparent owing to the reduction of 4-nitrophenol to 4 aminophenol. The color changes associated with the conversion of 4-nitrophenolate to 4-aminophenol enable one to easily monitor the reaction kinetics by UV–VIS spectroscopy. In order to estimate the product conversion, we employed a calibration curve for 4-nitrophenolate concentration as function of the absorbance at 400 nm. The catalytic activities of Au@Pd and AgPd hollow nanoflowers were described by TOF (turnover frequency) rates [39]. The TOF can be defined as the number of completed catalytic cycles per atom in catalytic surface of the catalyst as a function of time, and was calculated according to the Eq. 1:

$$\mathrm{TOF} = C_{4\mathrm{NP}}/(C_{\mathrm{M}} \cdot t), \quad (1)$$

where $C_{4\mathrm{NP}}$ denotes the concentration of 4-nitrophenolate converted to 4-aminophenol, C_{M} the total metal concentration, and t the time.

Synthesis of 1 wt% solid Au@Pd and hollow AgPd nanoflowers supported on silica

The solid Au@Pd and hollow AgPd nanoflowers were supported on commercial silica by a wet impregnation method at 1 wt% (in terms of total metal content) [40]. In typical experiment, 1 L of the nanoflowers suspension obtained after 30 min of reaction was concentrated to 50 mL. Then, 1 g of silica was added to resulting suspension and stirred vigorously at 80 °C until the formation of a paste. Then, 50 mL of distilled water was added and the suspension was kept under stirring to dryness (5 h). The catalysts were then treated at 120 °C for 2 h under air.

Catalytic activity toward benzene, toluene, and o-xylene oxidation (BTX oxidation)

The catalytic oxidation of BTX was performed in a fixed bed tubular quartz reactor under atmospheric pressure. The following conditions were chosen: 0.030 g catalyst, inlet benzene (1.2 g m^{-3}), toluene (0.7 g m^{-3}), *o*-xylene (0.5 g m^{-3}) in air, gas flow rate 20 cm^3 min^{-1}, residence time 0.3 s, gas hourly space velocity 12000 h^{-1}, and temperature range 25–300 °C. The reaction data were collected after at least 2 h on-stream at room temperature. The reaction products were determined by GC–MS. The reactant and product mixtures were analyzed using two online gas chromatographs equipped with FID and TCD detector and an HP-5 column. The catalytic activity was expressed as the degree of the conversion of BTX, respectively. The conversion of the BTX compounds was calculated as follows:

$$\mathrm{CBTXs}\ (\%) = \left[(\mathrm{BTXs})_{\mathrm{in}} - (\mathrm{BTXs})_{\mathrm{out}}\right] \times 100/(\mathrm{BTXs})_{\mathrm{in}}, \quad (2)$$

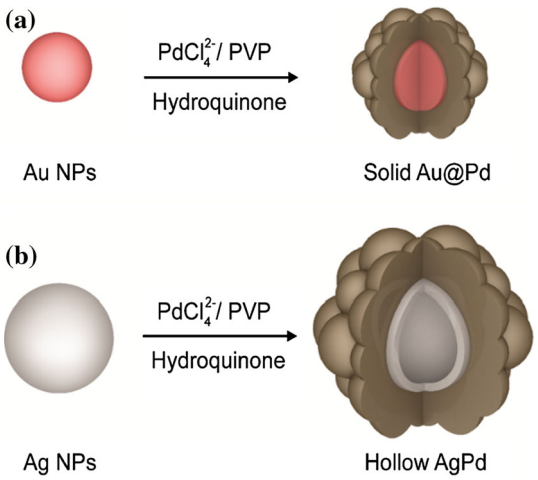

Scheme 1 Approach for the synthesis of solid Au@Pd and hollow AgPd nanoflowers. Solid Au@Pd nanoflowers (**a**) were obtained by the utilization of Au NPs as physical templates for Pd growth, while hollow AgPd nanoflowers (**b**) were obtained by the combination of the galvanic replacement reaction between Ag nanospheres and $PdCl_4^{2-}{}_{(aq)}$ and the reduction of $PdCl_4^{2-}{}_{(aq)}$ to Pd by hydroquinone

where CBTXs (%) is percentage of BTX conversion, $(BTXs)_{in}$ is input quantity, and $(BTXs)_{out}$ is output quantity.

Results and discussion

Materials characterization

Our studies started with the synthesis of solid Au@Pd and hollow AgPd nanoflowers as shown in Scheme 1. Solid Au@Pd nanoflowers could be obtained by a seed-mediated approach, in which Au NPs were employed as seeds (physical templates) for Pd growth in the presence of hydroquinone as the reducing agent (Scheme 1a) [19]. The synthesis of hollow AgPd nanoflowers, on the other hand, was based on the utilization of Ag NPs as chemical templates for Pd growth in the presence of hydroquinone. This approach is shown in Scheme 1b and combines the galvanic replacement reaction between Ag and $PdCl_4^{2-}{}_{(aq)}$ (which leads to the Ag oxidation and its subsequent dissolution from the core together with $PdCl_4^{2-}{}_{(aq)}$ reduction and deposition) and $PdCl_4^{2-}{}_{(aq)}$ reduction to Pd by hydroquinone (that contribute to the formation of the nanoflower morphology) [41].

Figure 1a shows a TEM image of Au NPs that were employed as seeds for the synthesis of Au@Pd nanoflowers. They were 15 ± 2 nm in diameter and displayed quasi-spherical shape. The Au@Pd nanoflowers obtained at different time intervals after the $PdCl_4^{2-}{}_{(aq)}$ addition to the reaction mixture containing the Au NPs seeds are shown in Fig. 1b–d. Our results show that the size of the Au@Pd nanoflowers could be controlled by varying the growth time before the $PdCl_4^{2-}{}_{(aq)}$ reduction to Pd was quenched by the addition of HCl to the reaction mixture. Specifically, Fig. 1b–d shows the Au@Pd materials obtained by quenching the $PdCl_4^{2-}{}_{(aq)}$ reduction after 15 s, 5 min, and 30 min of growth, respectively (a more detailed morphology evolution as a function of time is depicted in Figure S1). In all cases, the materials displayed quasi-spherical shape and were relatively monodisperse in size. The mass-thickness contrast detected from the TEM images confirms

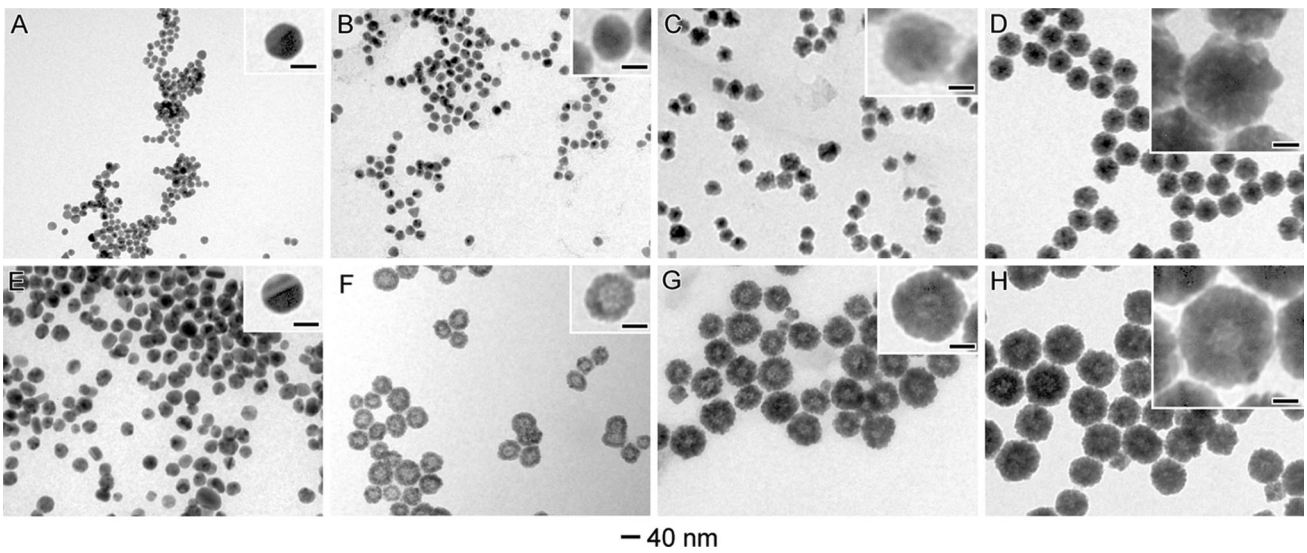

Fig. 1 **a–d** TEM images of Au NPs (**a**) employed as templates for the synthesis of solid Au@Pd nanoflowers (**b–d**) with controlled sizes as a function of the Pd growth time: 15 s (**b**), 5 min (**c**), and 30 min (**d**). (**e–h**) TEM images of Ag NPs (**e**) employed as templates for the synthesis of hollow AgPd nanoflowers (**f–h**) with controlled sizes by adjusting the Pd growth time: 15 s (**f**), 5 min (**g**), and 30 min (**h**). The *scale bars* in the *insets* correspond to 10 (**a–d**) or 20 nm (**e–h**)

the formation of an Au@Pd core–shell architecture. The size of the Au@Pd nanoflowers corresponded to 17 ± 2, 29 ± 3, and 39 ± 3 nm for 15 s, 5 min, and 30 min growth, respectively (corresponding to Pd shell thicknesses of 2 ± 0.3, 14 ± 2, and 25 ± 3 nm, respectively).

Figure 1e–h shows TEM images of Ag NPs seeds (Fig. 1e, 35 ± 4 nm in diameter) and the corresponding AgPd nanoflowers (Fig. 1f–h) obtained after the addition of $PdCl_4^{2-}{}_{(aq)}$ to the reaction mixture containing the Ag NPs at different time intervals (15 s, 5 min, and 30 min, respectively). The AgPd nanoflowers also displayed quasi-spherical shape and monodisperse sizes. The mass-thickness contrast from TEM images (Fig. 1f–h) clearly shows the formation of hollow interiors in all AgPd nanoflowers. As discussed for Au@Pd nanomaterials, the size of the hollow AgPd nanoflowers (Pd shell thickness) could also be tailored as a function of the growth time during the synthesis. Their outer diameters corresponded to 42 ± 3, 60 ± 5, and 77 ± 5 nm, when the growth time was 15 s, 5 min, and 30 min, respectively (Pd shell thicknesses of 8 ± 2, 26 ± 4, and 45 ± 4 nm, respectively). Here, the shell thickness in Au@Pd and AgPd nanoflowers is controlled by the growth time, the size of the Ag and Au NPs employed as seeds, and the method for Pd deposition. In the Au@Pd nanomaterials, Pd was deposited over the Au seeds only by precursor reduction in the presence of hydroquinone. However, for AgPd nanoflowers, Pd was deposited by both precursor reduction in the presence of hydroquinone and galvanic replacement reaction between Ag and $PdCl_4^{2-}$, which led to larger shell thicknesses relative to Au@Pd nanoflowers. Additional TEM images for AgPd nanoflowers are shown in Figure S2. The UV–VIS extinction properties of solid Au@Pd and hollow AgPd nanoflowers obtained at different growth times are in agreement with a formation of a Pd shell over the Au NPs and the Pd deposition accompanied by Ag oxidation and subsequent dissolution to yield hollow interiors (Fig. 2). The signal at 525 and 411 nm (for Au and Ag NPs, respectively) can be assigned to the dipole mode of the surface plasmon resonance (SPR) excitation [37, 38]. It can be observed that this signal disappears after 15 s growth in both materials in agreement with a formation of a Pd shell over the Au NPs and the Ag oxidation and subsequent dissolution to yield hollow interiors. Also, a strong signal at 246 nm appeared for both Au@Pd and AgPd nanoflowers after 15 s. Its signal intensity increased as function of time, and can be associated with the increased Pd deposition at the surface with time [19]. Interestingly, a band at 287 nm can also be observed in the Au@Pd and AgPd spectra. This signal is often related to the presence of free Pd clusters in suspension, which suggests that Pd growth may take place by cluster attachment [19]. For Au@Pd nanoflowers, this signal appeared after 15 s growth

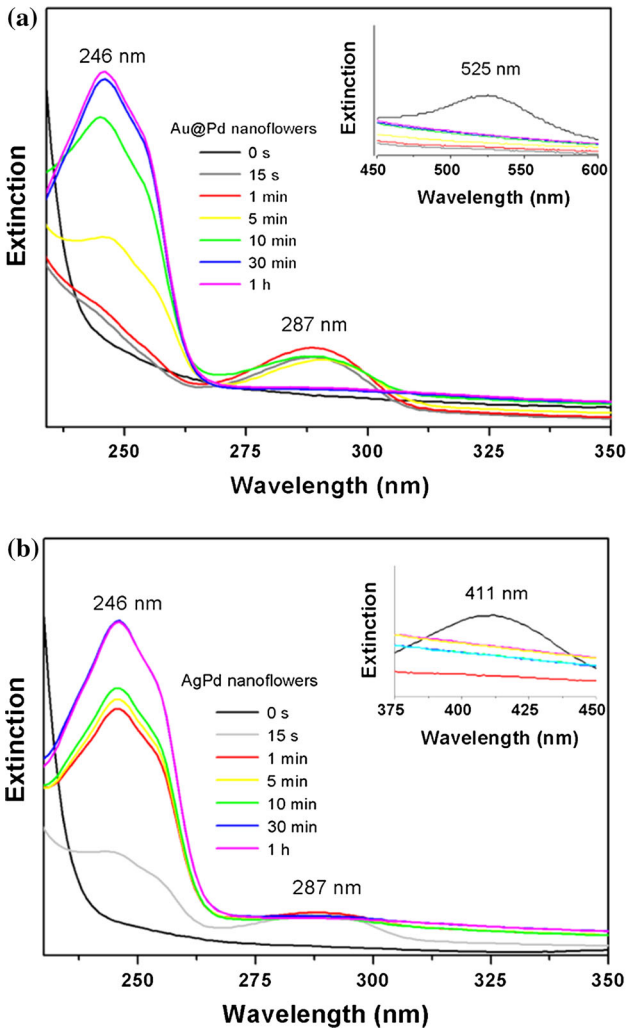

Fig. 2 UV-VIS extinction spectra as a function of reaction/growth time during the synthesis of Au@Pd (**a**) and AgPd (**b**) nanoflowers (Color figure online)

and then decreased in intensity only after 30 min. On the other hand, for AgPd nanoflowers, this peak was detected after 15 s growth and practically disappeared after 1 min. These observations agree with a faster reduction/growth kinetics for AgPd nanoflowers relative to Au@Pd, as Pd nucleation and growth are favored both by $PdCl_4^{2-}{}_{(aq)}$ reduction by hydroquinone and the galvanic replacement reaction between $PdCl_4^{2-}{}_{(aq)}$ and Ag. Figure S3 shows TEM images of the Au@Pd nanoflowers obtained without washing via successive steps of centrifugation and removal of the supernatant, which shows the presence of small Pd clusters together with the nanoflowers and indicates that Pd growth occurred by cluster attachment [19].

The compositional variations on Au@Pd and AgPd nanoflowers as a function of growth time determined FAAS (flame atomic absorption spectroscopy) analysis are shown in Tables S1 and S2, respectively. Specifically, the Pd at.% corresponded to 42, 73, and 88 in the Au@Pd and

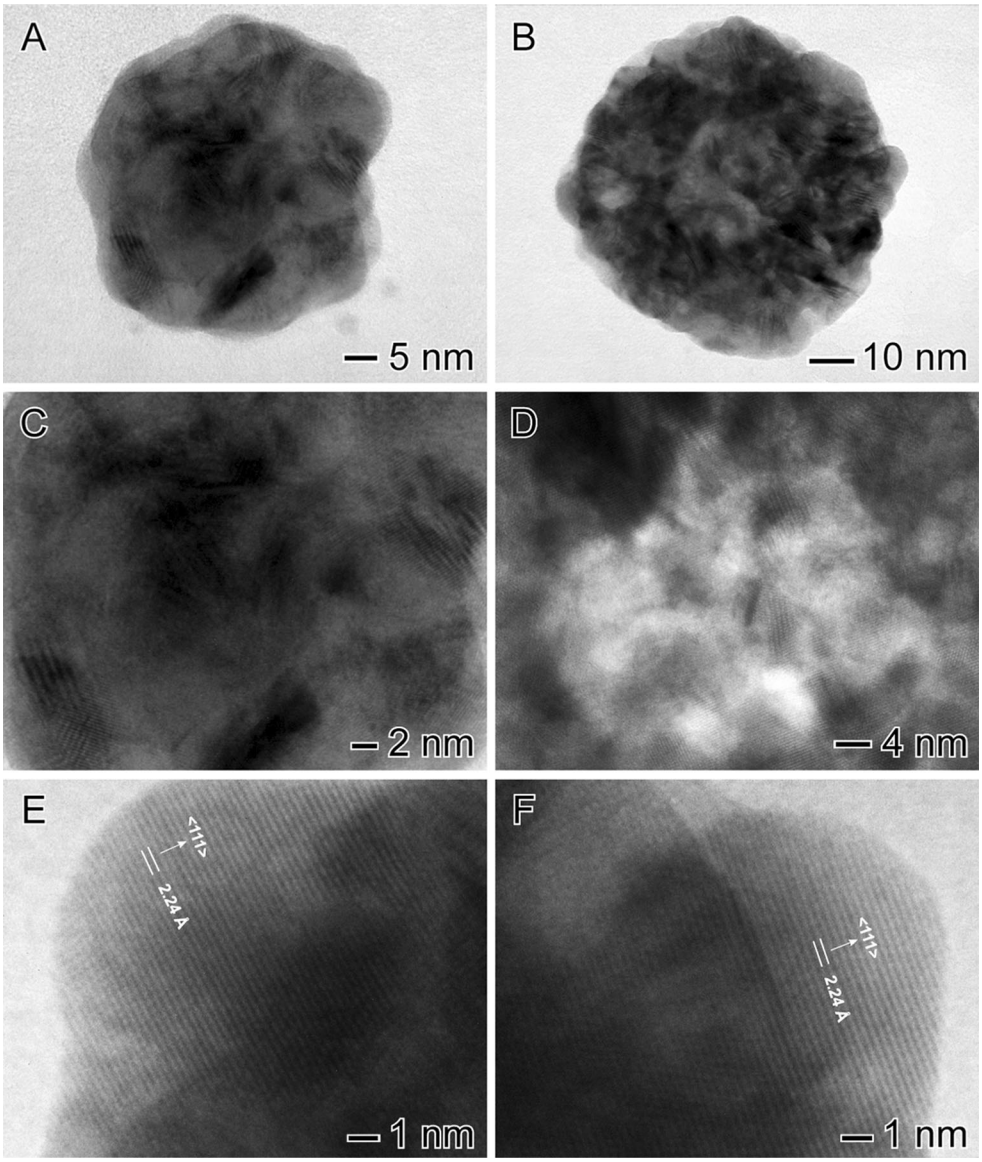

Fig. 3 HRTEM images for Au@Pd (**a**, **c**, and **e**) and AgPd (**b**, **d**, and **f**) nanoflowers obtained after 30 min growth. **a** and **b** show individual nanoflowers; **c** and **d** display their core regions; and **e** and **f** depict their shells. *Solid* and *hollow* interiors as well as single-crystalline Pd domains on their shells can be clearly observed from the images

to 62, 80, and 92 in the AgPd nanoflowers obtained after 15 s, 5 min, 30 min growth, respectively. Therefore, the Au@Pd and AgPd nanoflowers obtained after 15 s, 5 min, and 30 min growth could be denoted as $Au_{58}@Pd_{42}$, $Au_{27}@Pd_{73}$, and $Au_{12}@Pd_{88}$, respectively, and $Ag_{38}Pd_{62}$, $Ag_{20}Pd_{80}$, and $Ag_{8}Pd_{92}$, respectively. The increase in the Pd at.% as a function of time is in agreement with the growth of the Pd shells as illustrated by the TEM results.

Figure 3 shows HRTEM images for Au@Pd (Fig. 3a, c, and e) and AgPd (Fig. 3b, d, and f) nanoflowers obtained after 30 min growth. The images for individual nanoflowers (Fig. 3a and b) as well as zoom-in images for the core regions (Fig. 3c and d) clearly show the formation of solid or hollow interiors for Au@Pd and AgPd nanoflowers, respectively. Phase-contrast images for the shell regions (Fig. 3e and f) show the presence of Pd single-crystalline domains, in which the Pd {111} lattice fringes can be clearly visualized.

In order to unravel the role played by hydroquinone as a reducing agent to promote the formation of the nanoflower morphology, we performed a series of experiments regarding the synthesis of Au@Pd and AgPd nanostructures under the same experimental conditions as those describe in Fig. 1 by replacing hydroquinone with ascorbic acid, sodium borohydride, or sodium citrate. The effect of the reducing agent over the morphology of Au@Pd and

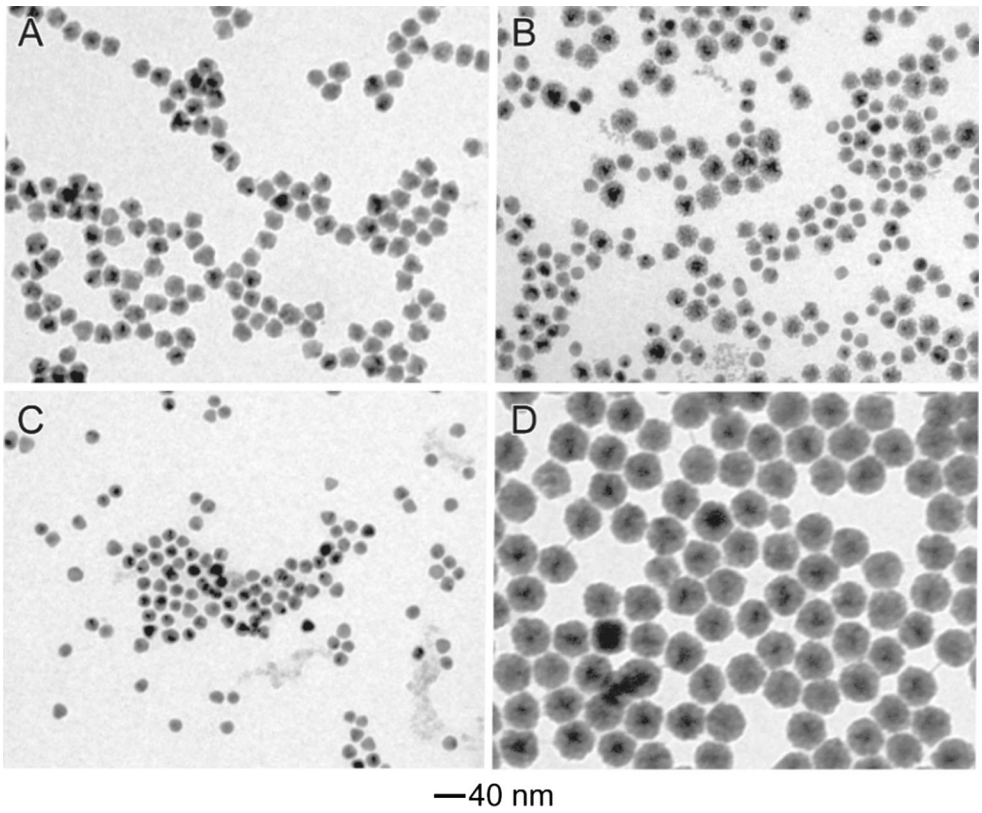

Fig. 4 TEM images of Au@Pd solid nanostructures obtained after 1 h growth by employing ascorbic acid (**a**) sodium borohydride (**b**), sodium citrate (**c**), and hydroquinone (**d**) as the reducing agents

AgPd materials results is shown in Figs. 4 and 5, respectively. The utilization of ascorbic acid as the reducing agent led to the formation of Au@Pd core–shell materials containing small bumps at the surface only after 1 h of reaction (Fig. 4a). When sodium borohydride was employed as a reducing agent, we could observe the formation of Au@Pd nanodendrites after 1 h (Fig. 4b). The presence of some uncoated nanoparticles and free Pd nanoparticles can be observed from the image. No Pd deposition was observed in the presence of sodium citrate (Fig. 4c). It is important to emphasize that the utilization of hydroquinone led to Au@Pd nanoflowers (after 1 h of growth, Fig. 4d) with outer diameters larger than those observed for Au@Pd materials obtained by using ascorbic acid and sodium borohydride. Regarding AgPd nanostructures, the formation of hollow nanoflowers was not detected when ascorbic acid, sodium borohydride, and sodium citrate were employed as reducing agents. Instead, the formation of AgPd nanoshells was observed (Fig. 5). Here, nanoshells refer to hollow nanomaterials having smooth surfaces, while nanodendrites refer to hollow nanostructures having branches or tips at their surface. Moreover, the formation of Pd clusters could also be detected in the images (Fig. 5b, c). These results demonstrate that the utilization hydroquinone is crucial to the formation of the nanoflower morphology in both Au@Pd and AgPd materials. These data also illustrate that the nature of the reducing agent (reducing strength) strongly affects the kinetics of Pd reduction. As citrate and ascorbic acid are weak reducing agents, it is plausible that they favor a layer-by-layer Pd deposition mechanism to give rise to core@shell (Au seeds) or hollow shell (Ag seeds) materials. On the other hand, sodium borohydride is a strong reducing agent, leading to a fast nucleation and growth kinetics of Pd over the templates and also contributing to the formation of isolated Pd NPs.

Catalytic performances

In the next step, we were interested in investigating how the catalytic activities of the solid Au@Pd and hollow AgPd nanoflowers were dependent upon size, composition, and nature of the cores (Au, Pd, and Ag represent active phases for this transformation). We started our catalytic studies by employing the reduction of 4-nitrophenol by sodium borohydride as a model reaction [13, 37, 42]. The calculated TOF (h^{-1}) rates for Au@Pd and AgPd nanoflowers obtained after 15 s, 1 min, and 30 min growth are depicted in Fig. 6 (Figure S4 depicts the kinetic profiles, and the pseudo first-order rate constants can be found

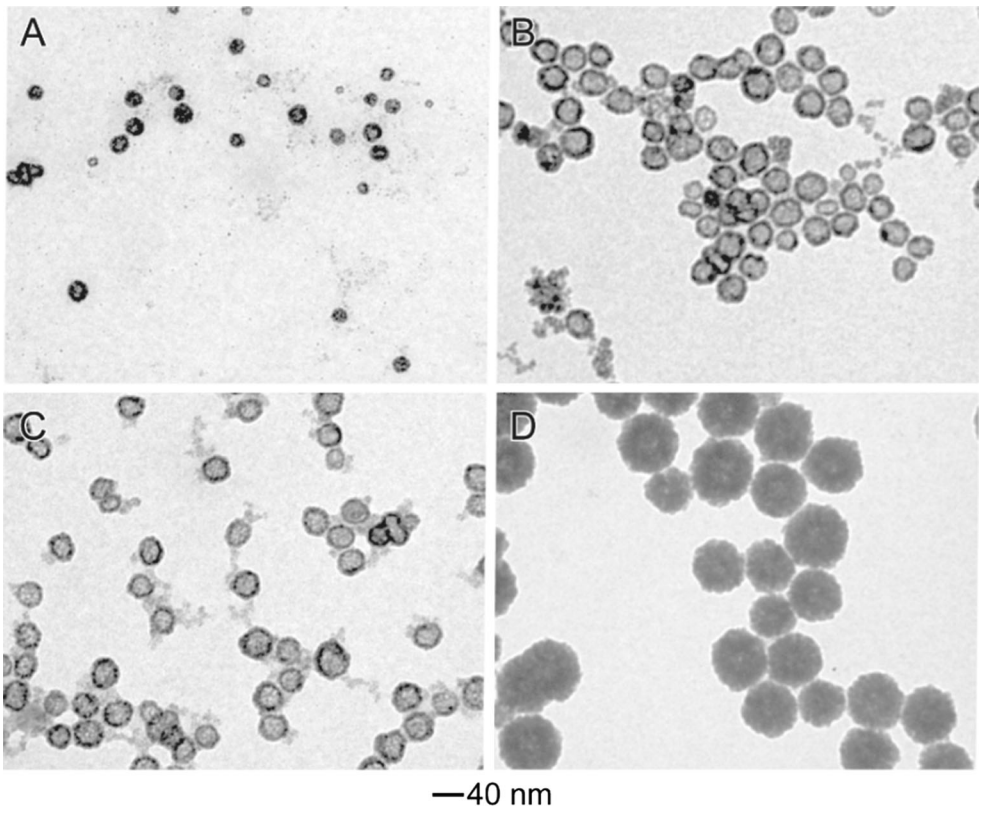

Fig. 5 TEM images of AgPd hollow nanostructures obtained after 1 h growth by employing ascorbic acid (**a**) sodium borohydride (**b**), sodium citrate (**c**), and hydroquinone (**d**) as the reducing agents

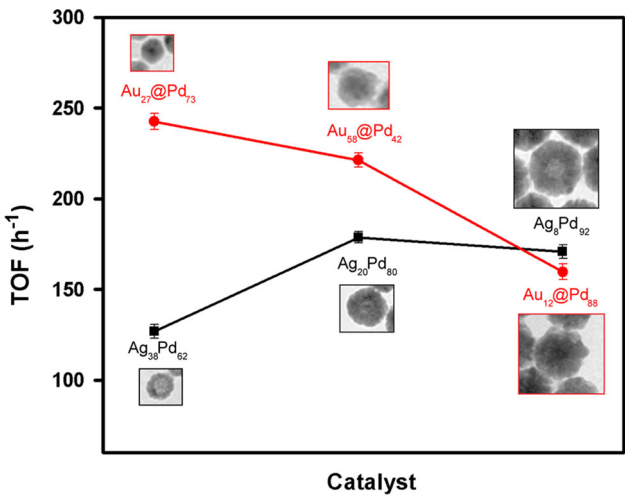

Fig. 6 Turnover frequencies values (TOF, h^{-1}) as a function of size/composition of solid Au@Pd (*red trace*) and hollow AgPd (*black trace*) nanoflowers as catalysts toward the 4-nitrophenol reduction (Color figure online)

in Table S3). The TOF rates at stationary state corresponded to 243 ± 4, 221 ± 3, and $160 \pm 5\ h^{-1}$ for $Au_{58}@Pd_{42}$, $Au_{27}@Pd_{73}$, and $Au_{12}@Pd_{88}$ materials, respectively. This indicates a decrease in the catalytic activity with the increase in the Au@Pd size, which might be related with the reduction in the surface area of the metal nanoparticles. Conversely, TOF values for AgPd nanoflowers corresponded to 127 ± 3, 179 ± 2, and $170 \pm 4\ h^{-1}$ for $Ag_{38}Pd_{62}$, $Ag_{20}Pd_{80}$, and Ag_8Pd_{92}, respectively. Interestingly, an increase in TOF values was detected with the increase in the AgPd size/shell thickness. These variations in TOF values can be explained as the Pd catalytic activity toward the 4-nitrophenolate reduction is higher relative to Ag [43]. Moreover, a synergic effect in bimetallic catalysts containing Au and Pd has been demonstrated for this reaction [44, 45]. Therefore, the Au contribution to the catalytic activity decreases as the Pd content in the nanoflowers increases in the Au@Pd material, leading to a decrease in TOF values with an increase in size and lower Au content. Here, it is plausible that it becomes harder for 4-nitrophenolate molecules to diffuse to the Au cores as the shell thickness was gradually increased. On the contrary, the increase in TOF values as a function of size for the AgPd nanoflowers may be explained by the gradual decrease in the Ag at % (which is less active than both Au and Pd) in the AgPd materials, despite the increase in size.

When we compare the solid Au@Pd and hollow AgPd nanoflowers, $Au_{58}@Pd_{42}$ and $Au_{27}@Pd_{73}$ materials displayed higher catalytic activities than $Ag_{38}Pd_{62}$ and

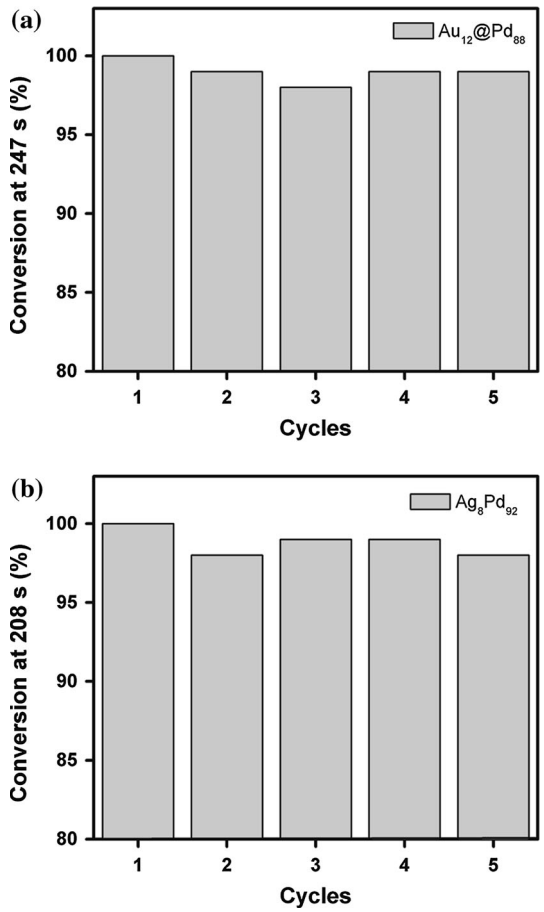

Fig. 7 Catalytic activity expressed in terms of 4-nitrophenol conversion as a function of number of catalytic cycles for **a** $Au_{12}@Pd_{88}$ and **b** Ag_8Pd_{92} nanoflowers

$Ag_{20}Pd_{80}$, respectively. It is plausible that the Au cores in the Au@Pd nanoflowers can contribute to improve the catalytic activities for 4-nitrophenolate reduction relative to the hollow AgPd material. As Au is much more active than Ag for this transformation, solid Au@Pd becomes better catalysts than hollow AgPd nanoflowers. Interestingly, at bigger sizes, in which the compositions become very similar ($Au_{12}@Pd_{88}$ and Ag_8Pd_{92} materials), hollow Ag_8Pd_{92} nanoflowers displayed slightly higher TOF values as compared to the solid $Au_{12}@Pd_{88}$ material, even though the Ag_8Pd_{92} nanoflowers have bigger outer diameters/shell thickness than to $Au_{12}@Pd_{88}$. This observation suggests that the hollow interiors contribute for improving the catalytic performance relative to the solid material at bigger sizes. We also performed control experiments in which we compared the catalytic activities toward the reduction of 4-nitrophenol of the AgPd and Au@Pd nanoflowers obtained after 30 min growth relative to monometallic Ag (Fig. 1a), Au (Fig. 1e), and Pd nanoparticles synthesized under the same experimental conditions as those describe in Fig. 1 without any seeds (Figure S5). The calculated TOF values (Figure S6) clearly show that the activity for both AgPd and Au@Pd nanoflowers was much higher relative to the sum of their individual monometallic nanoparticle counterparts, indicating that both Ag and Ag in the nanoflower structure contributed to the observed catalytic activities. Interestingly, our stability tests for the $Au_{12}@Pd_{88}$ and Ag_8Pd_{92} nanoflowers showed that they could be reused with no significant loss of activity even after 5 catalytic cycles (Fig. 7), indicating that they were stable under our employed conditions.

In order to further evaluate the role played by the nature of the cores, we decided to investigate the catalytic activity of the solid Au@Pd and hollow AgPd nanoflowers obtained after 30 min ($Au_{12}@Pd_{88}$ and Ag_8Pd_{92}) toward the gas-phase BTX oxidation. To this end, we scaled-up the synthesis of the nanoflowers by 100-folds and supported the resulting material onto commercial silica. It can be observed that the $Au_{12}@Pd_{88}$ and Ag_8Pd_{92} nanoflowers obtained after the scaled-up synthesis (Figure S7) displayed essentially the same morphology as those described in Fig. 1. The yield of AgPd nanoflowers was 89.7 and 85.5 % for the typical and scaled-up syntheses, respectively. For Au@Pd, these values corresponded to 92.1 and 87.7 %, respectively. The nanoflowers were then supported on silica by wet impregnation to generate $Au@Pd/SiO_2$ and $AgPd/SiO_2$ catalysts as shown Fig. 8a and b ($Au@Pd/SiO_2$) and Fig. 8c and d ($AgPd/SiO_2$). The concentrations in terms of metal of the nanoflowers suspensions employed for the preparation of the supported materials were 174 and 179 μM for AgPd and Au@Pd, respectively. The metal wt% in the supported catalysts was determined by FAAS. This approach enabled the uniform distribution (without agglomeration) of nanoflowers over the entire surface of the support. The metal loading in both materials corresponded to 1 % in weight.

Figure 9 depicts the conversion for the oxidation of BTX as a function of reaction temperature employing $Au@Pd/SiO_2$, $AgPd/SiO_2$, and pure SiO_2 as the catalysts (the inset in Fig. 9 shows a scheme for the BTX oxidation reaction). While no significant conversion was detected for the pure SiO_2 support, both $Au@Pd/SiO_2$ and $AgPd/SiO_2$ displayed good catalytic activities at relatively low temperatures. The oxidation of BTX began to take place at above 25, 50, and 75 °C, respectively. Only H_2O and CO_2 were detected as the oxidation products, and the BTX conversion increased with temperature for both $Au@Pd/SiO_2$ and $AgPd/SiO_2$ catalysts. Solid $Au@Pd/SiO_2$ was more active than the hollow $AgPd/SiO_2$ nanoflowers for the BTX oxidation reactions mainly at the higher temperatures. Specifically, 81 and 72 % conversion for benzene, 68 and 53 % conversion for toluene, and 41 and 36 % conversion for *o*-xylene were detected at 300 °C when $Au@Pd/SiO_2$ and $AgPd/SiO_2$ nanoflowers were employed as catalysts,

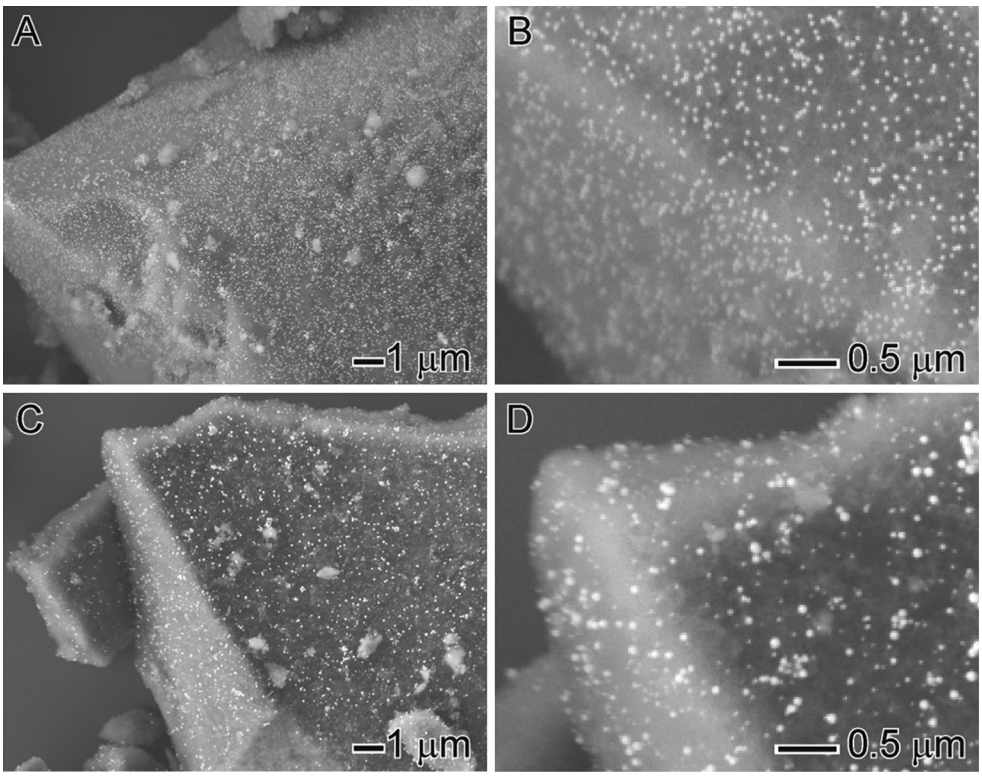

Fig. 8 SEM images of Au@Pd/SiO_2 (**a** and **b**) and AgPd/SiO_2 (**c** and **d**) materials obtained by the wet impregnation of Au@Pd and AgPd nanoflowers onto commercial SiO_2, illustrating the uniform dispersion of the nanoflowers over the silica support

respectively. Assuming the same noble metal content for both catalysts (1 wt%), the larger size of the hollow Ag_8Pd_{92} nanoflower can lead to a poorer dispersion on the SiO_2 support. Thus, the higher conversion percentages presented by the Au@Pd/SiO_2 catalyst can be explained by the better dispersion of the Au_{12}@Pd_{88} nanoflower on the SiO_2 support and also the fact that Au and Pd display higher catalytic activities than Ag toward the BTX oxidation (Fig. 8) [46]. Besides, the oxidation of organic compounds promoted by noble metal catalysts is recognized as a catalyst structure sensitive reaction [47]. As discussed for the 4-nitrophenol reduction, Au nanomaterials can also catalyze the BTX conversion. Therefore, it is plausible that, as the diffusion of gas molecules through the Pd shells in both Au@Pd and AgPd nanoflowers may be easier relative to liquid species, the Au core in the Au@Pd material can contribute to improve the catalytic activity toward BTX oxidation relative to the hollow AgPd nanoflowers. This shows that the nature and structure of the core can influence the catalytic performance in bimetallic core–shell architectures. For instance, a catalytically active core may contribute to boost the catalytic activity for a gas-phase reaction relative to the hollow (shell) material. Some authors have reported high catalytic activities for Au–Pd-based catalysts having a core–shell morphology (Au-rich core and a Pd-rich shell) toward oxidation reactions due to the synergetic effect between the noble metals [48, 49]. We believe that our results represent an important improvement in terms of performance relative to conventional systems. For instance, the conversion percentages reported in our paper are significantly higher (at lower metal loadings) as compared to conventional Au, Pd, and Au–Pd/SiO_2 catalysts employing the same experimental conditions [23]. Specifically, while $\sim$5 nm conventional Pd nanoparticles deposited over SiO_2 at 5 wt% loading having high dispersion displayed <50 % conversion toward the benzene oxidation at 300 °C, the Au@Pd and AgPd nanoflowers deposited over SiO_2 at 1 wt% loading displayed 81 and 72 % conversions at this temperature, respectively [23].

Conclusion

In summary, we described the synthesis of Au@Pd and AgPd nanoflowers displaying well-defined and controlled sizes, compositions, and structure (solid vs. hollow interiors), which enabled us to investigate how the presence of Au in the nanoflower's core affected their catalytic performance. Regarding the catalytic activities for the reduction of 4-nitrophenol, our data suggested that the Au in the core of the particles was capable of boosting the catalytic performance relative to the hollow material when the Pd

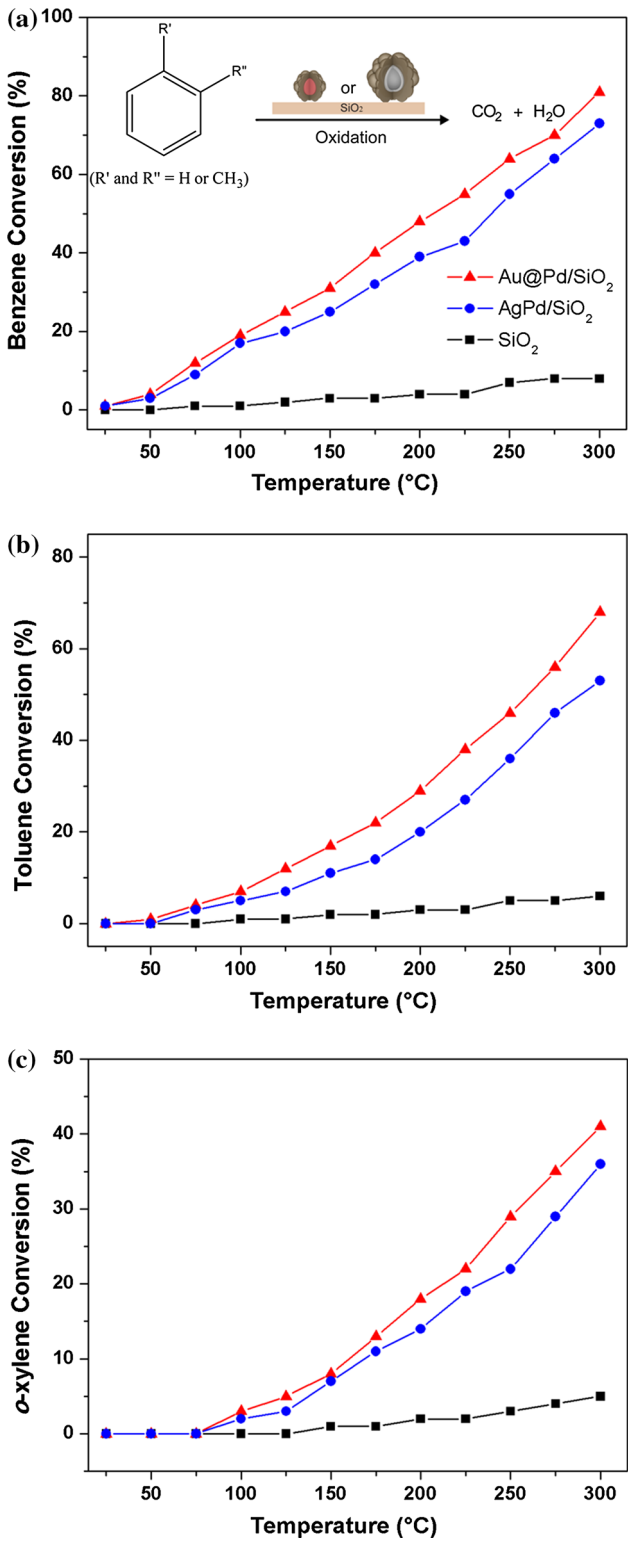

Fig. 9 Oxidation (conversion %) of benzene (**a**), toluene (**b**), and *o*-xylene (**c**) as a function of temperature catalyzed by $Au@Pd/SiO_2$, $AgPd/SiO_2$, and SiO_2 (*red*, *blue*, and *black traces*, respectively) (Color figure online)

at.% in the nanoflowers was up to 80. Above this value, the hollow Ag_8Pd_{92} nanoflowers had a slightly higher catalytic activity than the solid $Au_{12}@Pd_{88}$. On the contrary, solid $Au_{12}@Pd_{88}$ nanoflowers displayed higher catalytic activities toward the BTX oxidation as compared to the Ag_8Pd_{92} material. In this case, the Au content from the core of the nanoflowers could contribute to the catalytic activity even at higher Pd at.% values (larger sizes/shell thickness). These results indicate that the catalytic activities in core–shell and hollow systems are also sensitive to the type of reaction (liquid vs. gas phases). Therefore, we believe that our results may serve as a platform not only to the synthesis of bimetallic nanomaterials based on Pd displaying controlled compositions, architectures, and structures (both supported and unsupported), but also to understand how these parameters affect their catalytic activity for different classes of reactions.

Acknowledgements This work was supported by the Fundação de Amparo à Pesquisa do Estado de São Paulo (FAPESP) (Grant Number 2013/19861-6), the Conselho Nacional de Desenvolvimento Científico e Tecnológico (CNPq) (Grant Number 471245/2012-7). P. H. C. C. and H. V. F. thank the CNPq for the research fellowships. A. G. M. S., L. S. K. T., and T. S. R thank CNPq and CAPES for the fellowships.

Compliance with ethical standards

Conflict of Interest The authors declare that they have no conflict of interest.

References

1. Cheong S, Watt JD, Tilley RD (2010) Shape control of platinum and palladium nanoparticles for catalysis. Nanoscale 2:2045–2053
2. Yin Liebscher J (2006) Carbon–carbon coupling reactions catalyzed by heterogeneous palladium catalysts. Chem Rev 107: 133–173
3. Long R, Mao K, Ye X et al (2013) Surface facet of palladium nanocrystals: a key parameter to the activation of molecular oxygen for organic catalysis and cancer treatment. J Am Chem Soc 135:3200–3207
4. Speziali MG, da Silva AGM, de Miranda DMV et al (2013) Air stable ligandless heterogeneous catalyst systems based on Pd and Au supported in SiO_2 and MCM-41 for Suzuki–Miyaura cross-coupling in aqueous medium. Appl Catal A 462–463:39–45
5. Saldan I, Semenyuk Y, Marchuk I, Reshetnyak O (2015) Chemical synthesis and application of palladium nanoparticles. J Mater Sci 50:2337–2354
6. Da Silva AM, Robles-Dutenhefner P, Dias A et al (2013) Gold, palladium and gold–palladium supported on silica catalysts prepared by sol–gel method: synthesis, characterization and catalytic behavior in the ethanol steam reforming. J Sol-Gel Sci Technol 67:273–281
7. Crespo-Quesada M, Yarulin A, Jin M et al (2011) Structure sensitivity of alkynol hydrogenation on shape- and size-controlled palladium nanocrystals: which sites are most active and selective? J Am Chem Soc 133:12787–12794
8. Jin M, Zhang H, Xie Z, Xia Y (2012) Palladium nanocrystals enclosed by 100 and 111 facets in controlled proportions and their catalytic activities for formic acid oxidation. Energy Environ Sci 5:6352–6357

9. Slater TJA, Macedo A, Schroeder SLM et al (2014) Correlating catalytic activity of Ag–Au nanoparticles with 3D compositional variations. Nano Lett 14:1921–1926
10. Bai S, Wang X, Hu C et al (2014) Two-dimensional g-C3N4: an ideal platform for examining facet selectivity of metal co-catalysts in photocatalysis. Chem Commun 50:6094–6097
11. Long R, Zhou S, Wiley BJ, Xiong Y (2014) Oxidative etching for controlled synthesis of metal nanocrystals: atomic addition and subtraction. Chem Soc Rev 43:6288–6310
12. Rodrigues T, da Silva AM, Macedo A et al (2015) Probing the catalytic activity of bimetallic versus trimetallic nanoshells. J Mater Sci 50:5620–5629
13. Wang X, Fu J, Wang M et al (2014) Facile synthesis of Au nanoparticles supported on polyphosphazene functionalized carbon nanotubes for catalytic reduction of 4-nitrophenol. J Mater Sci 49:5056–5065
14. Lou XWD, Archer LA, Yang Z (2008) Hollow micro-/nanostructures: synthesis and applications. Adv Mater 20:3987–4019
15. Scott RWJ, Datye AK, Crooks RM (2003) Bimetallic palladium–platinum dendrimer-encapsulated catalysts. J Am Chem Soc 125:3708–3709
16. Wang D, Villa A, Porta F et al (2008) Bimetallic gold/palladium catalysts: correlation between nanostructure and synergistic effects. J Phys Chem C 112:8617–8622
17. Song HM, Anjum DH, Sougrat R et al (2012) Hollow Au@Pd and Au@Pt core-shell nanoparticles as electrocatalysts for ethanol oxidation reactions. J Mater Chem 22:25003–25010
18. Zhang S, Metin Ö, Su D, Sun S (2013) Monodisperse AgPd alloy nanoparticles and their superior catalysis for the dehydrogenation of formic acid. Angew Chem Int Ed 52:3681–3684
19. Xu J, Wilson AR, Rathmell AR et al (2011) Synthesis and catalytic properties of Au–Pd nanoflowers. ACS Nano 5:6119–6127
20. Kuai L, Yu X, Wang S et al (2012) Au–Pd alloy and core-shell nanostructures: one-pot coreduction preparation, formation mechanism, and electrochemical properties. Langmuir 28:7168–7173
21. Xiong Y, Xia Y (2007) Shape-controlled synthesis of metal nanostructures: the case of palladium. Adv Mater 19:3385–3391
22. Phan NTS, Van Der Sluys M, Jones CW (2006) On the nature of the active species in palladium catalyzed mizoroki-heck and suzuki-miyaura couplings—homogeneous or heterogeneous catalysis, a critical review. Adv Synth Catal 348:609–679
23. Da Silva AGM, Fajardo HV, Balzer R et al (2015) Versatile and efficient catalysts for energy and environmental processes: mesoporous silica containing Au, Pd and Au–Pd. J Power Sources 285:460–468
24. Lim B, Jiang M, Tao J et al (2009) Shape-controlled synthesis of Pd nanocrystals in aqueous solutions. Adv Funct Mater 19:189–200
25. Xia Y, Xiong Y, Lim B, Skrabalak SE (2009) Shape-controlled synthesis of metal nanocrystals: simple chemistry meets complex physics? Angew Chem Int Ed 48:60–103
26. Fu G, Wu K, Lin J et al (2013) One-pot water-based synthesis of Pt–Pd alloy nanoflowers and their superior electrocatalytic activity for the oxygen reduction reaction and remarkable methanol-tolerant ability in acid media. J Phys Chem C 117:9826–9834
27. Yin Z, Zheng H, Ma D, Bao X (2008) Porous palladium nanoflowers that have enhanced methanol electro-oxidation activity. J Phys Chem C 113:1001–1005
28. Mohanty A, Garg N, Jin R (2010) A universal approach to the synthesis of noble metal nanodendrites and their catalytic properties. Angew Chem Int Ed 49:4962–4966
29. Gao Q, Gao M-R, Liu J-W et al (2013) One-pot synthesis of branched palladium nanodendrites with superior electrocatalytic performance. Nanoscale 5:3202–3207
30. Damato TC, de Oliveira CCS, Ando RA, Camargo PHC (2013) A facile approach to TiO_2 colloidal spheres decorated with Au nanoparticles displaying well-defined sizes and uniform dispersion. Langmuir 29:1642–1649
31. Saha S, Pal A, Kundu S et al (2009) Photochemical green synthesis of calcium–alginate–stabilized Ag and Au nanoparticles and their catalytic application to 4-nitrophenol reduction. Langmuir 26:2885–2893
32. Khan FI, Ghoshal AK (2000) Removal of volatile organic compounds from polluted air. J Loss Prev Process Ind 13:527–545
33. Iranpour R, Cox HHJ, Deshusses MA, Schroeder ED (2005) Literature review of air pollution control biofilters and biotrickling filters for odor and volatile organic compound removal. Environ Prog 24:254–267
34. Everaert K, Baeyens J (2004) Catalytic combustion of volatile organic compounds. J Hazard Mater 109:113–139
35. Rezlescu N, Rezlescu E, Popa PD et al (2013) Nanostructured $GdAlO_3$ perovskite, a new possible catalyst for combustion of volatile organic compounds. J Mater Sci 48:4297–4304
36. Gennequin C, Lamallem M, Cousin R et al (2009) Total oxidation of volatile organic compounds on Au/Ce–Ti–O and Au/Ce–Ti–Zr–O mesoporous catalysts. J Mater Sci 44:6654–6662
37. da Silva AGM, Rodrigues TS, Macedo A et al (2014) An undergraduate level experiment on the synthesis of Au nanoparticles and their size-dependent optical and catalytic properties. Quím Nova 37:1716–1720
38. Silvert P-Y, Herrera-Urbina R, Duvauchelle N et al (1996) Preparation of colloidal silver dispersions by the polyol process. Part 1-synthesis and characterization. J Mater Chem 6:573–577
39. Boudart M (1995) Turnover rates in heterogeneous catalysis. Chem Rev 95:661–666
40. Jiang SP (2006) A review of wet impregnation—an alternative method for the fabrication of high performance and nano-structured electrodes of solid oxide fuel cells. Mater Sci Eng, A 418:199–210
41. da Silva AGM, de Souza ML, Rodrigues TS et al (2014) Rapid synthesis of hollow Ag–Au nanodendrites in 15 seconds by combining galvanic replacement and precursor reduction reactions. Chem Eur J 20:15040–15046
42. Wang S, Zhang J, Yuan P et al (2015) Au nanoparticle decorated N-containing polymer spheres: additive-free synthesis and remarkable catalytic behavior for reduction of 4-nitrophenol. J Mater Sci 50:1323–1332
43. Esumi K, Isono R, Yoshimura T (2003) Preparation of PAMAM- and PPI-metal (silver, platinum, and palladium) nanocomposites and their catalytic activities for reduction of 4-nitrophenol. Langmuir 20:237–243
44. Oh S-D, Kim M-R, Choi S-H et al (2008) Radiolytic synthesis of Pd–M (M = Ag, Au, Cu, Ni and Pt) alloy nanoparticles and their use in reduction of 4-nitrophenol. J Ind Eng Chem 14:687–692
45. Endo T, Kuno T, Yoshimura T, Esumi K (2005) Preparation and catalytic activity of Au–Pd, Au–Pt, and Pt–Pd binary metal dendrimer nanocomposites. J Nanosci Nanotechnol 5:1875–1882
46. Abbasi Z, Haghighi M, Fatehifar E, Saedy S (2011) Synthesis and physicochemical characterizations of nanostructured Pt/Al_2O_3–CeO_2 catalysts for total oxidation of VOCs. J Hazard Mater 186:1445–1454
47. Liotta LF (2010) Catalytic oxidation of volatile organic compounds on supported noble metals. Appl Catal B Environ 100:403–412
48. Hosseini M, Barakat T, Cousin R et al (2012) Catalytic performance of core–shell and alloy Pd–Au nanoparticles for total oxidation of VOC: the effect of metal deposition. Appl Catal B Environ 111–112:218–224
49. Enache DI, Barker D, Edwards JK et al (2007) Solvent-free oxidation of benzyl alcohol using titania-supported gold–palladium catalysts: effect of Au–Pd ratio on catalytic performance. Catal Today 122:407–411